NANO LETTERS
Letter
pubs.acs.org/NanoLett

Ionic Intercalation in Two-Dimensional van der Waals Materials: In Situ Characterization and Electrochemical Control of the Anisotropic Thermal Conductivity of Black Phosphorus

Joon Sang Kang, Ming Ke, and Yongjie Hu*

Department of Mechanical and Aerospace Engineering, University of California, Los Angeles, Los Angeles, California 90095, United States

Supporting Information

ABSTRACT: Two-dimensional van der Waals materials have shown novel fundamental properties and promise for wide applications. Here, we report for the first time an experimental demonstration of the in situ characterization and highly reversible control of the anisotropic thermal conductivity of black phosphorus. We develop a novel platform based on lithium ion batteries that integrates ultrafast optical spectroscopy and electrochemical control to investigate the interactions between lithium ions and the lattices of the black phosphorus electrode. We discover a strong dependence of the thermal conductivity on battery charge states (lithium concentrations) during the discharge/charge process. The thermal conductivity of black phosphorus is reversibly tunable over a wide range of 2.45−3.86, 62.67−85.80, and 21.66−27.58 W·m^{-1}·K^{-1} in the cross-plan, zigzag, and armchair directions, respectively. The modulation in thermal conductivity is attributed to phonon scattering introduced by the ionic intercalation in between the interspacing layers and shows anisotropic phonon scattering mechanism based on semiclassical model. At the fully discharged state ($x \sim 3$ in Li$_x$P), a dramatic reduction of thermal conductivity by up to 6 times from that of the pristine crystal has been observed. This study provides a unique approach to explore the fundamental energy transport involving lattices and ions in the layered structures and may open up new opportunities in controlling energy transport based on novel operation mechanisms and the rational design of nanostructures.

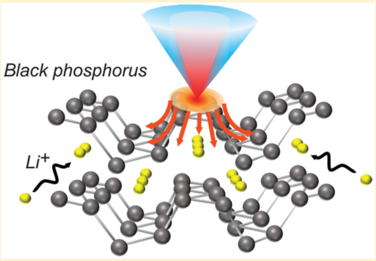

KEYWORDS: *2D van der Waals, anisotropic thermal conductivity, in situ thermal electrochemical measurement, black phosphorus, ion intercalation, phonon interaction*

Two-dimensional (2D) van der Waals (vdWs) materials have been of much interest in recent years due to their unique structures and properties.[1−4] In particular, black phosphorus (BP) is emerging as a promising new addition to the 2D vdWs family.[5] Although BP was first obtained back in 1914,[6] its unique in-plane anisotropy, widely tunable and direct bandgap, and high carrier mobility leads to a remarkable renaissance of interest for potential applications including electronics, photonics, and thermoelectric devices.[7−11] Moreover, with a high theoretical specific capacity BP has been explored as an attractive battery electrode material to store electrochemical energy though ionic intercalation.[12,13] However, the fundamental energy transport mechanism especially involving the coupled interactions between the intrinsic 2D lattices (i.e., phonons) and external ions during ionic intercalation process in the layered structures have not been well understood. In literature, the general concept of intercalation physics has been introduced and intensively studied for decades to achieve novel properties.[14] Very recent attempts were made to introduce intercalation in molybdenum disulfide for modulation.[15,16] Most studies so far require specific sample conditions or ex situ measurement. The anisotropic phonon interactions and in situ property control with high reversibility have not been demonstrated. In this work, we report for the first time an experimental demonstration of the in situ characterization on the anisotropic thermal properties of BP during ionic intercalation and demonstrate that the thermal conductivity of the 2D materials can be reversibly controlled through the ion−phonon interaction thanks to the unique phase structures of lithiated black phosphorus.

First, a high-quality BP film with a clean surface was prepared by mechanically exfoliating a high-purity BP crystal. Figure 1a shows the optical image of an exfoliated BP. This semiconducting BP is a layered material with a puckered orthorhombic crystal structure[17] (Figure 1b). Each layer includes two kinds of P−P bonds: the shorter bond connects the nearest P atoms in the same plane, and the longer bond connects P atoms in the top and bottom planes. Therefore, each P atom forms three covalent bonds mainly from 3p orbitals, and the interlayer interaction is based on van der Waals forces. Such a unique anisotropic crystal structure leads to anisotropic physical properties and is usually discussed based on three characteristic directions: the armchair (AC), zigzag direction (ZZ), and cross-plane (*c*) directions (Figure 1b).

Received: October 20, 2016
Revised: February 11, 2017
Published: February 23, 2017

DOI: 10.1021/acs.nanolett.6b04385
Nano Lett. 2017, 17, 1431−1438

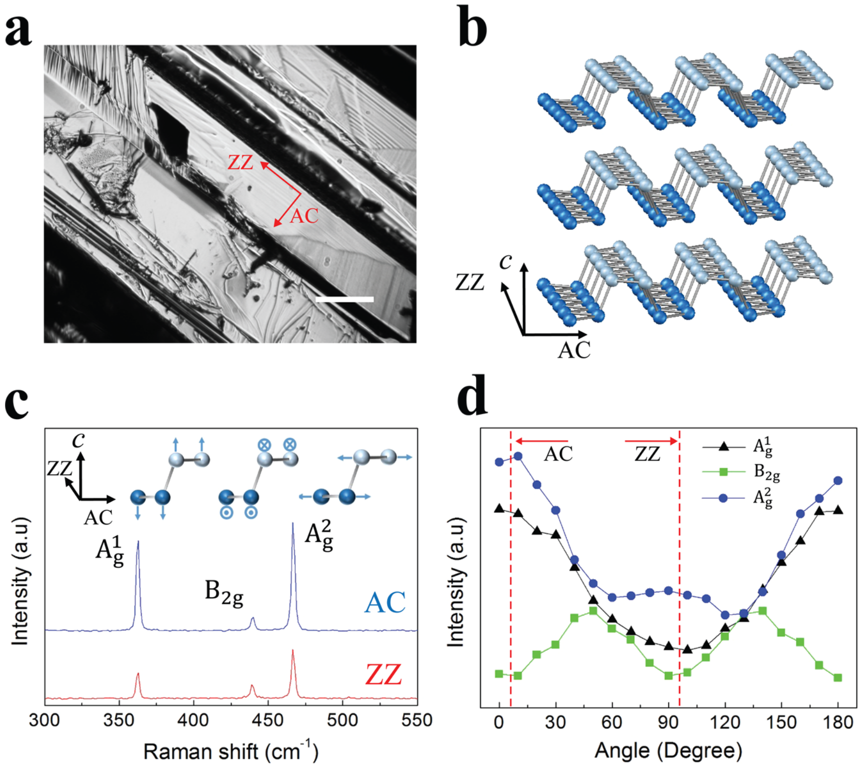

Figure 1. Crystal structure and material characterization of black phosphorus (BP). (a) Optical image of BP sample. The ZZ and AC directions are marked in the figure. The scale bar is 200 μm. (b) Schematic of BP crystal structure. The phosphorus atoms on the top and bottom plane are indicated as light blue and dark blue respectively. (c) Angle-dependent Raman spectroscopy of pristine BP. The blue and red data are measured when the Raman polarization is along the AC and ZZ direction, respectively. The inset schematics illustrate phonon vibration modes related to respective Raman peaks: A_g^1, B_{2g}, and A_g^2. (d) The intensity plot of the three Raman peaks with measurement angle dependence. The red dash lines indicate the AC and ZZ directions.

To identify the crystalline orientation and orient the BP sample for the following measurement, an angle-resolved, polarized Raman spectroscopy was performed. BP crystal has a D_{2h}^{18} point group and six active Raman vibration modes.[18] Under laser excitation along the *c*-plane, only three vibration modes will be detected due to the symmetric selection rule.[18,19] Figure 1c clearly shows that three active Raman peaks have been measured: A_g^1 (363 cm^{-1}), B_{2g} (440 cm^{-1}), and A_g^2 (467 cm^{-1}), and their corresponding vibration modes are illustrated in the schematic. The intensity of these Raman peaks depends on the alignment between the Raman polarization and the crystal orientations.[19] The A_g^2 peak intensity reaches the maximum when the Raman polarization is along the AC direction, whereas the B_{2g} peak is of the maximum intensity when Raman polarization is right in-between of the AC and ZZ directions. Figure 1d shows the relative intensity of each Raman peak with its associated angle-dependence. From this measurement, the AC and ZZ directions of BP samples are determined and marked in Figure 1d. In fact, the ZZ crystalline orientation corresponds to the stripe features naturally formed in the exfoliated BP (Figure 1a). In addition, no difference has been observed for Raman spectra performed at different spots of BP samples up to centimeter sizes, which indicates a very high crystalline quality and uniformity of these BP samples.

The thermal property of BP was characterized using a time-domain thermoreflectance (TDTR) technique,[20,21] as shown in Figure 2a (see Supporting Information). In this setup, a femtosecond laser pulse is split into a pump and a probe pulse. The pump pulse heats up the sample surface and creates an instantaneous temperature rise. The transient temperature decay due to this heat impulse is monitored by the probe pulse that is delayed in time with respect to the pump using a mechanical delay stage. The full transient decay curve can be fit with a multilayer thermal model to obtain the thermal conductivity (κ).[20,22,23] The cross-plane thermal conductivity (κ_c) of pristine BP was measured first. The experimental data from our TDTR measurement and fittings based on amplitude and phase signals are shown in Figure 2b,c, respectively. The amplitude and phase measurement demonstrated excellent agreement with each other and measured $\kappa_c = 3.86 \pm 0.41$ W·m^{-1}·K^{-1}. Such agreement is also confirmed by the sensitivity analysis of amplitude and phase measurement signals under present experimental conditions, indicating both fittings are reliable. Note that for the fitting of anisotropic materials, the anisotropic ratio of an in-plane thermal conductivity to a cross-plane conductivity is included in the thermal model. The cross-plane analysis was performed iteratively with the in-plane analysis.[24]

To examine the in-plane anisotropic property, we measured the thermal conductivity in the ZZ and AC directions (κ_{ZZ} and κ_{AC}, respectively) using beam offset TDTR (BO-TDTR) technique (see Supporting Information).[25] In BO-TDTR, the pump and probe beams are separated with an offset distance at the sample surface. The out-of-phase thermoreflectance signal (V_{out}) at short negative delay time (−50 ps) is used to determine the in-plane thermal conductivity. Figure 2d shows a two-dimensional data plot of V_{out} as a function of beam offset. The in-plane thermal conductivity along the ZZ and AC directions are obtained by fitting the full width at half-maximum (fwhm) of V_{out} over the beam offset distance along respective

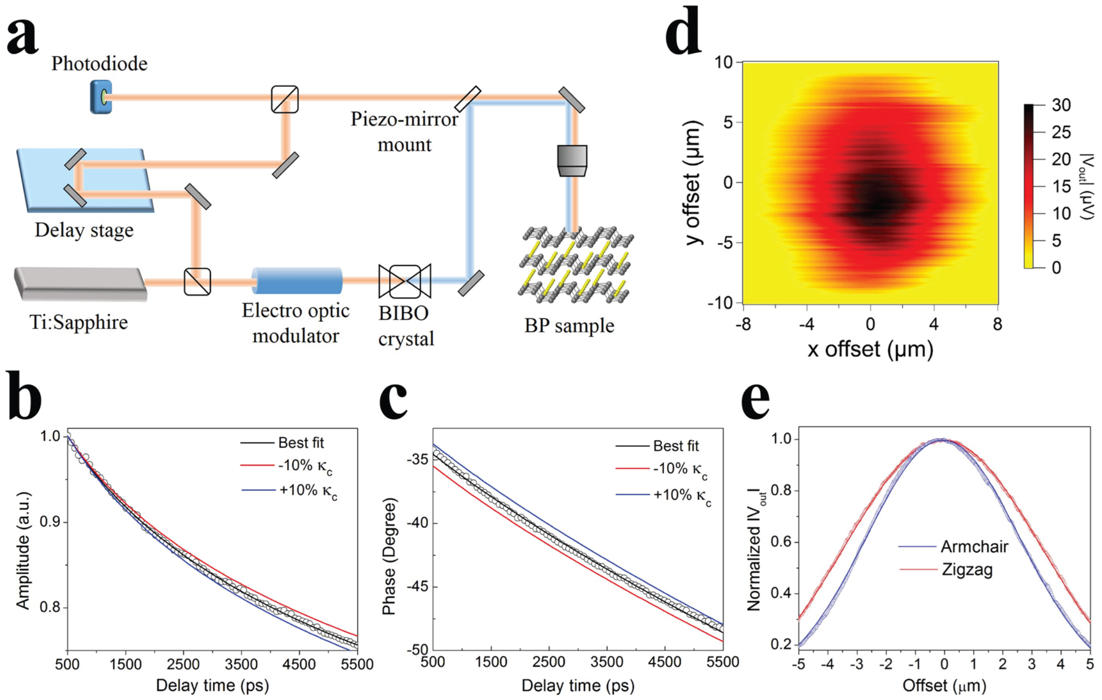

Figure 2. Experimental setup of the ultrafast pump−probe spectroscopy for measuring anisotropic thermal properties of pristine black phosphorus. (a) Schematic of TDTR spectroscopy for cross-plane thermal conductivity measurement. Blue and red color represents pump and probe beam, respectively. (b,c) Experimental measurement data and model fitting using both the (b) amplitude and (c) phase signals. Experimental data (black circles) and fits from the multilayer thermal transport model (black lines) for both the amplitude and phase signal. Calculated curves (red and blue lines) using the thermal conductivity changed by ±10% of best values are plotted to illustrate the measurement sensitivity. (d) BO-TDTR spectroscopy measurement of the in-plane thermal conductivity: two-dimensional mapping of the out-of-phase signal (V_{out}) is measured as a function of the offset distance between pump and probe laser beams. (e) In-plane thermal transport measurement of black phosphorus. Experimental data (circles) and fits from thermal transport model. The red color and blue color represents measurement in the armchair and zigzag direction, respectively.

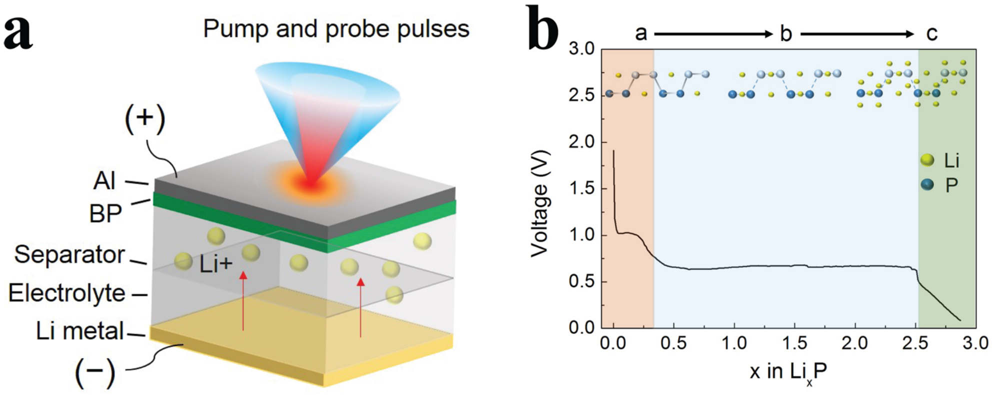

Figure 3. In situ thermal and electrochemical measurement. (a) Schematic of the in situ platform that integrates thermal transport using ultrafast optical spectroscopy with the electrochemical measurement. The device is based on a lithium ion battery and using black phosphorus as the battery electrode. (b) Galvanostatic discharge curve measured for the black phosphorus device. Inset: The schematic of a, b, and c illustrates structural evolution of black phosphorus during lithium intercalation, corresponding to the red, blue, and green background regimes, respectively.

directions. Typical experimental data from our BO-TDTR measurement and fittings are shown in Figure 2e. We used κ_c and interface conductance obtained from cross-plane measurement to extract κ_{ZZ} and κ_{AC}. The in-plane κ of pristine BP are measured to be κ_{ZZ} = 85.80 W·m^{-1}·K^{-1} and κ_{AC} = 27.58 W·m^{-1}·K^{-1}. The measured thermal conductivity of pristine BP is consistent with results in recent independent studies.[26−28]

To enable the in situ measurement and control of the thermal property of BP, we developed a novel electrochemical device platform (Figure 3a). The internal structure of our device represents a planar lithium ion battery configuration (see Supporting Information) where BP and lithium metal serve as the cathode and anode electrode, respectively. During the device operation (i.e., a battery discharging/charging process), the intercalation of Li atoms into and out from the interlayer spacing of the BP electrode is controlled using a BioLogic VSP-300 electrochemical workstation. The whole device with electrolyte was sealed inside a standard metal coin cell case to maintain the chemical stability. In addition, an optically transparent quartz window (1 mm × 1 mm) was fabricated on

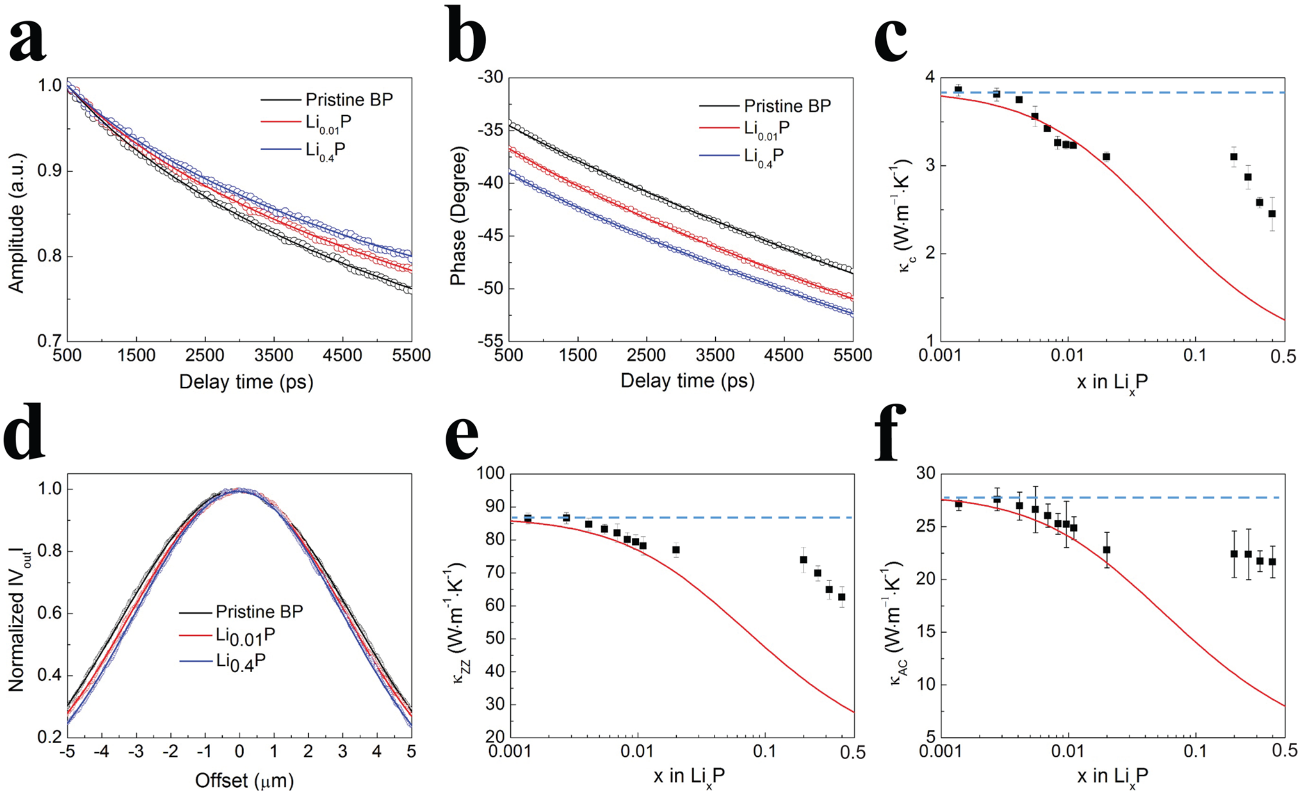

Figure 4. Measurement results of the anisotropic thermal conductivity at different lithium ion concentrations. (a,b) Experimental data for cross-plane thermal conductivity measurement based on the amplitude and phase signals (circles), and fits (solid line) from thermal model at different voltages. (c) The cross-plane thermal conductivity of black phosphorus is measured as a function of lithium concentrations during the battery discharge. Experimental data (solid rectangulars) is plot with the fit based on Callaway model (red line). The thermal conductivity of the pristine sample is marked in blue dashed line. (d) Experimental data (V_{out}) (circles) for in-plane thermal conductivity measurement and fits from thermal model at three different lithium concentrations. (e,f) The in-plane thermal conductivity (zigzag and armchair direction, respectively) of black phosphorus is measured as a function of lithium concentrations during the battery discharge. Experimental data (solid rectangulars) is plot with the fit based on Callaway model (red line). The thermal conductivity of the pristine sample is marked in blue dashed line.

the metal case to allow in situ TDTR spectroscopy to probe the BP surface while simultaneously controlling the ionic intercalation.

The electrochemical device serves as an excellent platform to investigate the dynamics of Li intercalation into BP film and the resulting structural evolution. A pristine BP film typically shows an open circuit voltage between 1.9 and 2.2 V with respect to Li/Li^+. We carried out Li interaction by gradually reducing the BP potential with respect to Li/Li^+. A typical galvanostatic discharge curve of the discharge potential versus lithium concentration (represented by x in Li_xP) is shown in Figure 3b. Evolution in the Li_xP structure (insert in Figure 3b) during discharge consists of the following three major regimes: (a) The first regime, highlighted in red, corresponds to physical intercalation of lithium ions. Initially, a steep drop in potential is observed due to change in the battery internal resistance.[29] The first plateau appears near 1.0 V, where a mixture of metastable Li_xP phases forms. Recent literature[30−32] reported that despite the appearance of these phases the lattice still maintains a 2D-like structure with minimum volume change (represented as the structure a in the inset of Figure 3b). Discharge continues until the lithium slots are completely filled. Li ions enter the BP structure through the channels running in the zigzag direction and settles in between P atoms.[13] Li intercalation is more preferentially aligned with ZZ direction due to the large difference in diffusion energy barriers in these two directions[33] (i.e., 0.68 and 0.08 eV for AC and ZZ, respectively). In this regime, lithium ions involve physical intercalation into the interlayer spacing without forming chemical bonding with the BP lattice. (b) As more Li is driven into Li_xP the large attraction force between Li and P pulls on the P−P bounds until the bounds break, causing the alloy formation of LiP[34] (structure b). The second regime, highlighted in blue, marks the first break down of the P−P bounds. Once the battery is discharged beyond this point, the P−P bounds cannot be recovered. The discharge curve reaches the second plateau when the new LiP alloy phase is established. At the end of this stage, the available slots for accommodating Li in structure b are all occupied. (c) Further introducing Li ions after saturation will induce another pull on the yet unbroken P−P bounds. This change (from structure b to structure c) is accompanied by another drop in voltage, and the discharge curve enters the third regime. In the third regime, highlighted in green, LiP undergoes another alloy formation process. Alternating layers of LiP and Li_2 appear until the ultimate formation of Li_3P[35] (structure c in the inset). Significant expansion in both lateral and longitudinal direction has been reported after complete discharge.[36] Therefore, for the in situ thermal measurement we first focus on charging/discharging the battery in the first regime to maintain a reversible BP structure and device performance.

The cross-plane thermal conductivity of BP was measured in situ during lithium interaction using TDTR. Typical experimental data of the transient TDTR amplitude and phase signal are shown in Figure 4a,b, respectively. In addition, examples of measurement data at different lithium concentrations (x = 0, 0.01, and 0.4 in $\mathrm{Li}_x\mathrm{P}$) are plotted together to illustrate the contrast in transport behaviors. Consistent results of κ_c are obtained by fitting amplitude and phase data using thermal diffusion modeling and are shown in Figure 4c. The κ_c of BP reduces gradually with increasing ionic intercalation. For example, κ_c is measured to be 3.24 ± 0.10 $\mathrm{W \cdot m^{-1} \cdot K^{-1}}$ for $\mathrm{Li}_{0.01}\mathrm{P}$ and 2.45 ± 0.19 $\mathrm{W \cdot m^{-1} \cdot K^{-1}}$ for $\mathrm{Li}_{0.4}\mathrm{P}$. The total drop of κ_c from pristine BP to $\mathrm{Li}_{0.4}\mathrm{P}$ is 37%.

The in-plane thermal conductivity of BP was measured in situ during lithium interaction using BO-TDTR. Typical experimental data of the out-phase signal V_{out} at different charge states (x = 0, x = 0.01, and x = 0.4 in $\mathrm{Li}_x\mathrm{P}$) along the ZZ direction are shown in Figure 4d. The thermal conductivity in the ZZ direction are κ_{ZZ} = 85.80, 79.33, and 62.67 $\mathrm{W \cdot m^{-1} \cdot K^{-1}}$, respectively for the three charge states after fitting with the obtained experimental data. Figure 4e,f shows the charge state dependence of κ_{ZZ} and κ_{AC}, respectively. The in-plane κ reduces as more Li enters the interlayer spacing in BP. κ_{ZZ} at x = 0.4 is about 28% less than that of the pristine BP. A similar trend in the ionic modulation of the thermal conductivity along the AC direction has been observed in experiment (Figure 4f). For example, κ_{AC} are found to be 27.58, 25.23, and 21.66 $\mathrm{W \cdot m^{-1} \cdot K^{-1}}$ at x = 0, 0.01, and 0.4, respectively. The total thermal conductivity drop in the AC direction is 21%.

It is interesting to note that such a reduction of the in-plane thermal conductivity of BP, although impressive, is relatively small in comparison to previous studies on other 2D materials.[37,38] For example, a significant thermal conductivity reduction (from ~2500 to ~370 $\mathrm{W \cdot m^{-1} \cdot K^{-1}}$) from suspended to substrate-supported graphene has been observed at room temperature[38] due to interactions between the substrate and graphene. On the other hand, the lithium ions here intercalated in the interlayer spacing and sandwiched between 2D layers, intuitively are expected to produce stronger scattering than that from the interaction with the substrate. However, a much less reduction in thermal conductivity is measured in the BP samples. We attribute such difference to the following mechanisms: First, BP has a relatively larger interlayer space (~5 Å) to accommodate the intercalation of lithium ions (1.52 Å) and minimize structure distortion.[13] Second, the relative contribution to thermal conductivity from varied phonon vibration modes is different in BP versus graphene. Generally, the heat in 2D materials can be carried by three different phonon modes: out-of-phase acoustic (ZA), longitudinal acoustic (LA), and transverse acoustic (TA), among which ZA is most affected by ambient scattering such as scattering from the substrate or due to the ion intercalation. ZA mode contribution to the in-plane thermal conductivity of graphene is large and reported to be more higher than 75%.[37,39] In contrary, recent first principle calculations have predicted that ZA phonon in BP only carries 12–31% of the in-plane thermal conductivity.[40] Our experimental results confirm that BP is less susceptible than graphene under ambient scattering.

To elucidate the physical mechanism behind the thermal conductivity reduction due to ionic intercalation, the semi-classical Callaway model[41] is used to analyze our experimental results. The thermal conductivity derived by Callaway model is expressed by

$$\kappa = \frac{k_B}{2\pi^2 v}\left(\frac{k_B}{\hbar}\right)^3 T^3 \int_0^{\theta_D/T} \frac{\chi^4 e^{\chi}}{(e^{\chi}-1)^2}\tau \, d\chi \tag{1}$$

where v, T, k_B, θ_D, and $\hbar$ are the phonon group velocity, the sample temperature, the Boltzmann constant, Debye temperature, and the Plank constant, respectively. The dimensionless parameter χ is define as $\hbar\omega/k_BT$ and ω is the phonon frequency. The total phonon relaxation time (τ) is contributed by Rayleigh scattering (τ_r) from impurities, anharmonic (Umklapp) phonon scattering (τ_a), and grain boundary scattering (τ_b), following the Matthiessen rule[41]

$$\tau^{-1} = \tau_r^{-1} + \tau_a^{-1} + \tau_b^{-1} = A\omega^4 + B\omega^2 + \frac{v}{L} \tag{2}$$

where L is the grain size, and A and B are numerical coefficient related with Rayleigh and anharmonic scattering. The first Rayleigh scattering term is related to impurity scattering (both mass and lattice fluctuation).[42] The second anharmonic scattering term is temperature dependent phonon–phonon scattering. Here the coefficient B can be considered at the high temperature regime ($T > \theta_D$), where B is proportional to temperature, $B \sim T$. The third boundary scattering term depends on sample grain size or characteristic length. For the single crystal BP sample, boundary scattering is considered negligible.

Therefore, at the high temperature regime eq 1 can be expressed as[43]

$$\kappa = \frac{k_B{}^2 T^3 \hbar}{2\pi^2 v} \int_0^{\theta_D/T} \frac{\chi^2 e^{\chi}}{T^2 (A k_B{}^2 T^2 \chi^2 + B)(e^{\chi}-1)^2} \, d\chi \tag{3}$$

At high temperature limit ($\chi < 1$), $\frac{\chi^2 e^{\chi}}{(e^{\chi}-1)^2} \sim 1$, then[43]

$$\kappa = \frac{k_B}{2v\pi^2 (AB)^{0.5}} \tan^{-1}\left[\frac{k_B \theta_D}{\hbar}\left(\frac{A}{B}\right)^{0.5}\right] \tag{4}$$

For the pristine BP (i.e., A → 0)), the thermal conductivity is related to the coefficient B by

$$\kappa_0 = \frac{k_B{}^2 \theta_D}{2\pi^2 v \hbar B} \tag{5}$$

Thus, the value of B (the coefficient of anharmonic scattering term) can be directly calculated from the experimentally measured κ_0 value.

The Rayleigh coefficient A can be further expressed in two items to describe mass disorder and lattice disorder[44] and is

$$A = \frac{\Omega_o}{4\pi v^3}(\Gamma_m + \Gamma_l) = \frac{\Omega_o}{4\pi v^3} c(1-c)\left(\left(\frac{\Delta M}{M_{avg}}\right)^2 + \varepsilon\left(\frac{\Delta r}{r_{avg}}\right)^2\right) \tag{6}$$

where the Ω_o is the unit cell volume, and Γ_m and Γ_l are scaling parameters to descript mass disorder and lattice disorder, respectively. c is the relative impurity concentration of $\mathrm{Li}_x\mathrm{P}$ and can be calculated as $c = \frac{x}{1+x}$. ΔM is the mass difference between BP atom and Li ion, M_{avg} is the average mass of compound, Δr is the atomic radius different between BP and Li, and r_{avg} is the average atomic radius. The mass disorder term is directly calculated with respect to function of Li ions. To describe lattice disorder, phenomenological adjustable parameter, ε, is introduced to be determined by experimental fitting, which is a function of Grüneisen parameter by strain

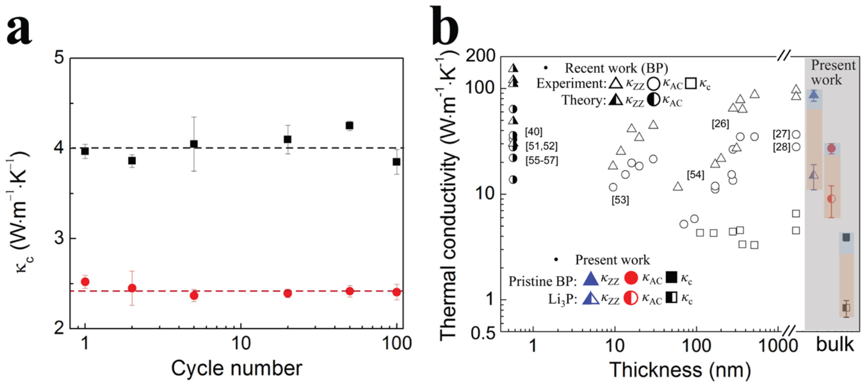

Figure 5. Reversibility measurement of the thermal regulation and summary of thermal conductivities of black phosphorus. (a) Thermal conductivity is measured as a function of battery charge/discharge cycles. For each cycle, the cross-plane thermal conductivity is measured for fully charged state (rectangles at $V = 2.0$ V and circles at $V = 0.78$ V). The average values of the maximum and minimum thermal conductivity over 100 charge cycles are marked in black and red dash lines. (b) Summary of thermal conductivity measurement in three different directions and plotted in comparison to reported values as a function of thickness. Results from this work are highlighted on the right side in the figure. Thermal conductivities of black phosphorus for the zigzag (blue), the armchair (red), and cross-plane (black) are plotted to illustrate the thermal regulation range from the fully charged state (filled symbols) to fully discharged state (half-filled symbols). Reversible and irreversible regime for thermal regulation is marked in blue and red background, respectively.

fluctuation.[45] Therefore, after A and B are replaced with eqs 6 and 5, respectively, ε is the only fitting parameter for thermal conductivity in eq 4. We fit our experimental results using the derived Callaway model.

The fitting results from semiclassical Callaway model is shown in Figure 4c,e,f. In the low concentration regime ($x < 0.1$), the model agrees well with our experimental results. The fitted value of ε along cross-plane and in-plane direction is different. For cross-plane direction, ε is fitted to be ~40, which is consistent with literature expectation,[44] and indicates that Li intercalation between BP layer introduces lattice distortion to the cross-plane direction. On the other hand, the ε value is ~1 for both in-plane directions that indicates that in-plane lattice distortion is not as important, whereas the large mass difference between Li ion and P atom (~5 times) provides the major contribution to impurity scattering.

In the high Li concentration regime ($x > 0.1$), however, model fitting is deviated from experiment despite of any choice of ε values. Interestingly, such discrepancy is consistent with the metastable phases between BP and LiP predicted by recent theoretical study.[46] In addition, because Callaway model is derived for isotropic material such as silicon, it may not be able to capture the anisotropic properties of BP. We expect future improvement of theoretical model using first-principle methods[47] and including anisotropic characteristics[48] will provide better understanding of our experimental data.

To check the reversibility of the electrochemical control over thermal conductivity, we performed in situ measurement over battery charging/discharging up to 100 cycles. Figure 5a shows a cycling measurement on κ_c for pristine BP and $Li_{0.4}P$, corresponding to 2.0 and 0.78 V, respectively. We use 0.05C current rate for battery cycling to minimize crystalline distortion of BP. During 100 cycling, κ_c variations at 2.0 and 0.78 V are within measurement uncertainty range, which are 3.86–4.25 W·m^{-1}·K^{-1} (2.0 V) and 2.36–2.52 W·m^{-1}·K^{-1} (0.78 V). The results show that the electrochemical tuning of thermal conductivity is highly reversible: the modulation of κ_c maintains ~40% between the two state (i.e., $x = 0$ and 0.4 in Li_xP) up to 100 cycles. This dynamic and reversible tunability of κ in layered material in fact demonstrates a novel ionic gate thermal transistor[49] that controls thermal conductivity with ON/OFF switching capability.

Our study has demonstrated a novel electrochemical approach to reversibly control thermal conductivity through in situ ionic intercalation. In addition to measurement in the first reversible regime of BP, we also measured the κ of the fully discharged sample (Li_3P). In this irreversible regime, the measured κ_c, κ_{AC}, and κ_{ZZ} are 0.84 ± 0.25, 9.25 ± 3.18, and 15.57 ± 4.98 W·m^{-1}·K^{-1}, respectively. The measured thermal conductivity of Li_3P is remarkably lower than pristine BP. Impressively, it gives the factors of 5, 3, and 6 times the tunability of κ_c, κ_{AC}, and κ_{ZZ}, respectively. The origin of the low thermal conductivity comes from the crystallinity of BP that is damaged by Li intercalation and single crystal BP is transformed into polycrystalline Li_3P. Consistently, the recently reported in situ XRD measurement reveals that the BP single crystal has been irreversibly transformed to a polycrystalline Li_3P in the fully discharge state.[50] Figure 5b summarizes the thermal conductivity values of BP from our study and the literature.[26−28,40,51−57] The reversible and irreversible thermal conductivity tuning regime is shown in the Figure 5b. It covers remarkably a large thermal conductivity tuning range and shows that Li ion intercalation can be a powerful method for thermal conductivity tuning.

In summary, we reported for the first time an active and reversible tuning of thermal conductivity of 2D materials using Li ion intercalation. A unique in situ measurement platform for modulating thermal property during electrochemical intercalation was developed. The pristine and voltage-dependent κ variations in BP are found to be highly anisotropic with values in the reversible regime ($0 < x < 0.4$ in Li_xP) varying from 2.45–3.86, 62.67–85.80, and 21.66–27.58 W·m^{-1}·K^{-1} in the cross-plane, ZZ, and AC directions, respectively. The difference in reduction is as high as 37%. Moreover, at the fully discharged state ($x \sim 3$ in Li_xP), the measured κ_c, κ_{ZZ}, and κ_{AC} are 0.84, 9.25, and 15.57 W·m^{-1}·K^{-1}, respectively, demonstrating an ultrahigh tunability of κ at factors of ~5, 3, and 6 times. These results reveal an effective mechanism for modifying the thermal conductivity of 2D materials based on electrochemical intercalation and phase transitions, and a novel approach to control anisotropic energy transport by designing nanostructures. In addition, it may open up a new direction for engineering thermal properties through mapping, scattering, and manipulating the phonon spectra in a rational way.[20,58]

■ ASSOCIATED CONTENT

Ⓢ Supporting Information

The Supporting Information is available free of charge on the ACS Publications website at DOI: 10.1021/acs.nanolett.6b04385.

Details of battery fabrication, electrochemical measurement, and thermal conductivity measurement (PDF)

■ AUTHOR INFORMATION

Corresponding Author

*E-mail: yhu@seas.ucla.edu.

ORCID

Yongjie Hu: 0000-0001-7225-1130

Notes

The authors declare no competing financial interest.

■ ACKNOWLEDGMENTS

Y.H. acknowledges support from the Young Investigator Award through the United States Air Force Office of Scientific Research and the Sustainable LA Grand Challenge and the Anthony and Jeanne Pritzker Family Foundation.

■ REFERENCES

(1) Zhang, Y.; Tan, Y. W.; Stormer, H. L.; Kim, P. *Nature* **2005**, *438* (7065), 201−204.

(2) Novoselov, K. S.; Geim, A. K.; Morozov, S. V.; Jiang, D.; Katsnelson, M. I.; Grigorieva, I. V.; Dubonos, S. V.; Firsov, A. A. *Nature* **2005**, *438* (7065), 197−200.

(3) Geim, A. K.; Grigorieva, I. V. *Nature* **2013**, *499* (7459), 419−425.

(4) Novoselov, K. S.; Mishchenko, A.; Carvalho, A.; Neto, A. H. C.; Road, O. *Science* **2016**, *353* (6298), aac9439.

(5) Ling, X.; Wang, H.; Huang, S.; Xia, F.; Dresselhaus, M. S. *Proc. Natl. Acad. Sci. U. S. A.* **2015**, *112* (15), 4523.

(6) Bridgman, P. W. *J. Am. Chem. Soc.* **1914**, *36* (7), 1344−1363.

(7) Li, L.; Yu, Y.; Ye, G. J.; Ge, Q.; Ou, X.; Wu, H.; Feng, D.; Chen, X. H.; Zhang, Y. *Nat. Nanotechnol.* **2014**, *9* (5), 372−377.

(8) Xia, F.; Wang, H.; Jia, Y. *Nat. Commun.* **2014**, *5*, 4458.

(9) Wang, H.; Wang, X.; Xia, F.; Wang, L.; Jiang, H.; Xia, Q.; Chin, M. L.; Dubey, M.; Han, S. J. *Nano Lett.* **2014**, *14* (11), 6424−6429.

(10) Wang, X.; Jones, A. M.; Seyler, K. L.; Tran, V.; Jia, Y.; Zhao, H.; Wang, H.; Yang, L.; Xu, X.; Xia, F. *Nat. Nanotechnol.* **2015**, *10* (6), 517−521.

(11) Fei, R.; Faghaninia, A.; Soklaski, R.; Yan, J.; Lo, C.; Yang, L. *Nano Lett.* **2014**, *14* (11), 6393−6399.

(12) Qian, J.; Wu, X.; Cao, Y.; Ai, X.; Yang, H. *Angew. Chem.* **2013**, *125* (17), 4731−4734.

(13) Sun, J.; Lee, H.-W.; Pasta, M.; Yuan, H.; Zheng, G.; Sun, Y.; Li, Y.; Cui, Y. *Nat. Nanotechnol.* **2015**, *10* (11), 980−985.

(14) Dresselhaus, M. S.; Dresselhaus, G. *Adv. Phys.* **2002**, *51* (1), 1−186.

(15) Xiong, F.; Wang, H.; Liu, X.; Sun, J.; Brongersma, M.; Pop, E.; Cui, Y. *Nano Lett.* **2015**, *15* (10), 6777−6784.

(16) Zhu, G.; Liu, J.; Zheng, Q.; Zhang, R.; Li, D.; Banerjee, D.; Cahill, D. G. *Nat. Commun.* **2016**, *7*, 13211.

(17) Morita, A. *Appl. Phys. A: Solids Surf.* **1986**, *39* (4), 227−242.

(18) Sugai, S.; Shirotani, I. *Solid State Commun.* **1985**, *53* (9), 753−755.

(19) Wu, J.; Mao, N.; Xie, L.; Xu, H.; Zhang, J. *Angew. Chem., Int. Ed.* **2015**, *54* (8), 2366−2369.

(20) Hu, Y.; Zeng, L.; Minnich, A. J.; Dresselhaus, M. S.; Chen, G. *Nat. Nanotechnol.* **2015**, *10* (8), 701−706.

(21) Zeng, L.; Collins, K. C.; Hu, Y.; Luckyanova, M. N.; Maznev, A. A.; Huberman, S.; Chiloyan, V.; Zhou, J.; Huang, X.; Nelson, K. A.; Chen, G. *Sci. Rep.* **2015**, *5*, 17131.

(22) Cahill, D. G. *Rev. Sci. Instrum.* **2004**, *75* (12), 5119−5122.

(23) Schmidt, A. J.; Chen, X.; Chen, G. *Rev. Sci. Instrum.* **2008**, *79* (11), 114902.

(24) Feser, J. P.; Liu, J.; Cahill, D. G. *Rev. Sci. Instrum.* **2014**, *85*, 104903.

(25) Feser, J. P.; Cahill, D. G. *Rev. Sci. Instrum.* **2012**, *83* (10), 104901.

(26) Jang, H.; Wood, J. D.; Ryder, C. R.; Hersam, M. C.; Cahill, D. G. *Adv. Mater.* **2015**, *27* (48), 8017−8022.

(27) Sun, B.; Zeng, Q.; Huang, X.; Liu, Z.; Kan Koh, Y.2016, arXiv:1606.05984.

(28) Zhu, J.; Park, H.; Chen, J.-Y.; Gu, X.; Zhang, H.; Karthikeyan, S.; Wendel, N.; Campbell, S. A.; Dawber, M.; Du, X.; Li, M.; Wang, J.-P.; Yang, R.; Wang, X. *Adv. Electron. Mater.* **2016**.

(29) Bard, A. J.; Faulkner, L. R. *Electrochemical Methods*, 2nd ed.; Wiley, 2001.

(30) Zhao, S. J.; Kang, W.; Xue, J. M. *J. Mater. Chem. A* **2014**, *2* (44), 19046−19052.

(31) Li, Q. F.; Duan, C. G.; Wan, X. G.; Kuo, J. L. *J. Phys. Chem. C* **2015**, *119* (16), 8662−8670.

(32) Zhang, C.; Anderson, G.; Dharmasena, R. R.; Sumanasekera, G.; Yu, M. 2016, arXiv: 1607.00317.

(33) Li, W.; Yang, Y.; Zhang, G.; Zhang, Y. W. *Nano Lett.* **2015**, *15* (3), 1691−1697.

(34) Park, C.-M.; Sohn, H.-J. *Adv. Mater.* **2007**, *19* (18), 2465−2468.

(35) Nazri, G. A.; Julien, C.; Mavi, H. S. *Solid State Ionics* **1994**, *70−71*, 137−143.

(36) Sun, J.; Zheng, G.; Lee, H. W.; Liu, N.; Wang, H.; Yao, H.; Yang, W.; Cui, Y. *Nano Lett.* **2014**, *14* (8), 4573−4580.

(37) Seol, J. H.; Jo, I.; Moore, A. L.; Lindsay, L.; Aitken, Z. H.; Pettes, M. T.; Li, X.; Yao, Z.; Huang, R.; Broido, D.; Mingo, N.; Ruoff, R. S.; Shi, L. *Science* **2010**, *328* (5975), 213−216.

(38) Cai, W.; Moore, A. L.; Zhu, Y.; Li, X.; Chen, S.; Shi, L.; Ruoff, R. S. *Nano Lett.* **2010**, *10* (5), 1645−1651.

(39) Lindsay, L.; Li, W.; Carrete, J.; Mingo, N.; Broido, D. A.; Reinecke, T. L. *Phys. Rev. B: Condens. Matter Mater. Phys.* **2014**, *89* (15), 1−8.

(40) Jain, A.; McGaughey, A. J. H. *Sci. Rep.* **2015**, *5*, 8501.

(41) Callaway, J. *Phys. Rev.* **1959**, *113* (4), 1046−1051.

(42) Luckyanova, M. N.; Chen, D.; Ma, W.; Tuller, H. L.; Chen, G.; Yildiz, B. *Appl. Phys. Lett.* **2014**, *104* (6), 061911.

(43) Callaway, J.; vonBaeyer, H. *Phys. Rev.* **1960**, *120* (4), 1149−1154.

(44) Abeles, B. *Phys. Rev.* **1963**, *131* (5), 1906−1911.

(45) Zhou, Z.; Uher, C.; Jewell, A.; Caillat, T. *Phys. Rev. B: Condens. Matter Mater. Phys.* **2005**, *71* (23), 1−6.

(46) Mayo, M.; Griffith, K. J.; Pickard, C. J.; Morris, A. J. *Chem. Mater.* **2016**, *28* (7), 2011−2021.

(47) (a) Regner, K. T.; Sellan, D. P.; Su, Z.; Amon, C. H.; McGaughey, A. J. H.; Malen, J. *Nat. Commun.* **2013**, *4*, 1640. (b) Esfarjani, K.; Chen, G.; Stokes, H. T. *Phys. Rev. B: Condens. Matter Mater. Phys.* **2011**, *84* (8), 1−11. (c) Broido, D. A.; Malorny, M.; Birner, G.; Mingo, N.; Stewart, D. A. *Appl. Phys. Lett.* **2007**, *91* (23), 231922. (d) Feng, T.; Qiu, B.; Ruan, X. *Phys. Rev. B: Condens. Matter Mater. Phys.* **2015**, *92* (23), 1−5. (e) Parker, D.; Singh, D. J. *J. Appl. Phys.* **2010**, *108* (8), 083712.

(48) Chen, Z.; Wei, Z.; Chen, Y.; Dames, C. *Phys. Rev. B: Condens. Matter Mater. Phys.* **2013**, *87* (12), 1−14.

(49) Li, B.; Wang, L.; Casati, G. *Appl. Phys. Lett.* **2006**, *88* (14), 143501.

(50) Xu, F.; Ge, B.; Chen, J.; Nathan, A.; Xin, L. L.; Ma, H.; Min, H.; Zhu, C.; Xia, W.; Li, Z.; Li, S.; Yu, K.; Wu, L.; Cui, Y.; Sun, L.; Zhu, Y. *2D Mater.* **2016**, *3* (2), 025005.

(51) Qin, G. Z.; Yan, Q. B.; Qin, Z. Z.; Yue, S. Y.; Hu, M.; Su, G. *Phys. Chem. Chem. Phys.* **2015**, *17* (7), 4854−4858.

(52) Liu, T. H.; Chang, C. C. *Nanoscale* **2015**, *7* (24), 10648−10654.

(53) Luo, Z.; Maassen, J.; Deng, Y.; Du, Y.; Lundstrom, M. S.; Ye, P. D.; Xu, X. *Nat. Commun.* **2015**, *6*, 8572.
(54) Lee, S.; Yang, F.; Suh, J.; Yang, S.; Lee, Y.; Li, G.; Sung Choe, H.; Suslu, A.; Chen, Y.; Ko, C.; Park, J.; Liu, K.; Li, J.; Hippalgaonkar, K.; Urban, J. J.; Tongay, S.; Wu, J. *Nat. Commun.* **2015**, *6*, 8573.
(55) Hong, Y.; Zhang, J.; Huang, X.; Zeng, X. C. *Nanoscale* **2015**, *7*, 18716−18724.
(56) Xu, W.; Zhu, L.; Cai, Y.; Zhang, G.; Li, B. *J. Appl. Phys.* **2015**, *117* (21), 214308.
(57) Zhang, J.; Liu, H. J.; Cheng, L.; Wei, J.; Liang, J. H.; Fan, D. D.; Jiang, P. H.; Shi, J. 2016, arXiv:1601.07302.
(58) Maldovan, M. *Nature* **2013**, *503* (7475), 209−217.

DOI: 10.1021/acs.nanolett.6b04385
Nano Lett. 2017, 17, 1431−1438